RSC Advances

PAPER

View Article Online
View Journal | View Issue

Cite this: *RSC Adv.*, 2025, **15**, 26412

Recent advances in electrochemical monitoring for the detection of the chemical oilfield tracer carmine

Nuerbiya Yalikun, *[a] Tianyi Huo,[a] Hongzhou Gong,[a] Buayixiemu Musa[a] and Guangzhi Hu *[b]

Accurate and efficient detection of chemical oilfield tracers is essential for enhanced oilfield geological analyses. We report the development of an electrochemical sensor for detecting carmine (CM) using coal tar pitch secondary residue (CTPSI) as a carbon precursor. Porous carbon materials derived from CTPSI (CTPSI-PC) were synthesized through high-temperature carbonization and strong-alkali activation. The CTPSI-PC material had high specific surface area, excellent conductivity, and a dense porous structure. Under optimized conditions, the constructed sensor demonstrated good electrochemical performance for CM detection, with a wide linear range of 10–200 μM, high sensitivity of 5.7324 A L cm^2 mol^{-1}, and a low limit of detection of 0.017 μM (S/N = 3). In real oilfield water samples, the recovery rate was 99.4% and 103.2%, showing excellent reproducibility, stability, and selectivity against common interfering ions. These findings highlight the potential of CTPSI-PC-based electrochemical sensors as efficient and reliable tools for quantitative detection of oilfield tracers, and lays a foundation for practical applications in oilfield monitoring.

Received 16th May 2025
Accepted 8th July 2025

DOI: 10.1039/d5ra03456f

rsc.li/rsc-advances

1. Introduction

Oilfield tracers are essential tools in petroleum exploration. There are many types of oilfield tracers, and the commonly used gas tracers have the disadvantages of complex preparation process, expense, and environmentally unfriendliness, which restricts their utility. Common chemical tracers such as organic dyes, fluorescein, SCN, Br, and ethanol, which are inexpensive, readily available, and have excellent chemical, physical, and biological stabilities, widely used in oilfield tracing.[1] Among them, carmine red (CM) has the characteristics of being odorless as well as being resistant to light, acids, and heat. It is used in various fields, such as food, dye, and petroleum industries, and can be used as an oilfield tracer for evaluating reservoir geology.[2–4] Therefore, CM is crucial for the detection of chemical tracers.

Recent advances in material science, particularly the development of carbon-based electrode materials such as coal-based porous carbon, have significantly enhanced the performance of electrochemical sensors. Coal tar pitch (CTP) is produced as a byproduct during the processing of coal tar in industry.[5] Using CTP as a basic carbon source, the components and synthetic process can be adjusted to produce porous carbon materials with different morphologies and excellent properties, such as large specific surface area, high electrical conductivity, and dense porous structure.[6] However, due to the complex composition of CTP, there are many impurities, which will lead to the poor electrochemical performance of carbon materials.[7,8]

Based on solubility parameters, the optimal extractants are selected and CTP is extracted stepwise. After stepwise extraction, the light components in CTP are removed. Then, the hydrogen and oxygen contents are reduced, and the degree of aromatic-ring condensation is increased, thereby obtaining better precursors for porous carbon materials. The latter demonstrate significant feasibility for electrochemical sensing applications,[9,10] providing novel pathways for commercializing CTP-derived carbon sensors.[11,12] This approach can realize the secondary utilization of CTP as a high value-added resource.[13–15]

Hansen developed "Hansen Solubility Parameter Software" (HSPiP) based on the solubility effect of solvents on materials.[16] The HSP of the material can be quickly and accurately simulated and calculated using a computational model of a generic algorithm for analytical fitting. In HSP theory, the total solubility parameter (δ_t) of the material to be measured consists of three components: polar solubility parameter (δ_P), dispersive solubility parameter (δ_D), and hydrogen bonding solubility parameter (δ_H). This approach provides reliable theoretical

[a]*State Key laboratory of Chemistry and Utilization of Carbon Based Energy Resources, Xinjiang Key Laboratory of Coal Cleaning Conversion & Chemical Engineering, Xinjiang Uyghur Autonomous Region, School of Chemical Engineering and Technology, Xinjiang University, Urumqi, Xinjiang, 830017, P. R. China. E-mail: nuerbiya@xju.edu.cn; Fax: +86 991 8582966; Tel: +86 991 8582966*

[b]*School of Ecology and Environmental Science, Qilu Lake Field Scientific Observation and Research Station for Plateau Shallow Lake in Yunnan Province, Ecological Research and Pollution Control of Plateau Lakes, Yunnan University, Kunming 650504, China*

support for extractant selection and separation of coal bitumen.[17,18]

CTP-based porous carbon (CTP-PC) materials are widely used in scientific research and practical applications because of their high specific surface area and readily controllable surface chemistry.[19,20] Combined with high electrical conductivity, high thermal conductivity,[21] high chemical stability and low density of coal bituminous carbon materials, and a wide range of sources of low cost, CTP-derived carbon materials can provide high levels of electrical and thermal conductivities, stability, and low density.[22] They show great potential for applications in CO_2 adsorption, catalysis, hydrogen storage, electrochemical sensors, lithium cathodes, as well as electrochemical bilayer capacitors and fuel cells.[23]

Oilfield tracer technology involves injecting tracers into reservoirs to monitor formation connectivity, flow dynamics, and production efficiency.[24] Among chemical tracers, carmine is extensively applied in geological analyses due to its stability and detectability,[25,26] so it is crucial for the rapid detection of CM. Traditionally, the detection of chemical oilfield tracers has relied on spectrophotometry, chromatography, capillary electrophoresis, and fluorescence analyses.[27] These methods are widely used and offer reliable results, but they often involve complex procedures, extended analytical times, and high operational costs, highlighting the need for more efficient alternatives.[28,29]

Electroanalytical methods have gained significant attention for carmine detection in recent years. These methods are simple, cost-effective, sensitive, and amenable to miniaturization, making them highly competitive tools for oilfield tracer analysis.[30–35] The integration of advanced materials, such as CTPSI-derived porous carbon, further enhances the sensitivity and selectivity of electrochemical sensors, providing a practical alternative to conventional methods.

We employed HSPiP software to simulate the solubility parameters of CTP, and selected ethanol and toluene as extractants for stepwise extraction. Through this process, primary (CTPPI) and secondary (CTPSI) residues were obtained and characterized using Fourier transform infrared (FT-IR) spectroscopy to analyze their chemical structures. The CTPSI was utilized as a carbon precursor to prepare CTPSI-PC through high-temperature carbonization and template methods. These materials were subsequently employed to modify electrodes, enabling preparation of an electrochemical sensor for CM detection. The electrochemical performance and electrocatalytic mechanism of the sensor were systematically investigated.

2 Experimental details

2.1 Instruments and reagents

All chemicals were of analytical grade and used without purification. CTP (high temperature) was from Hami Naomao Lak in Xinjiang (China). Oilfield water was from Lun nan Oilfield TK25KH in Xinjiang. Before application, they underwent vacuum filtration to remove sediment and large particles. $K_3[Fe(CN)_6]$, carmine, HCl, Na_2HPO_4, NaOH, NaH_2PO_4, KOH, KCl, H_2O, $K_4[Fe(CN)_6]$, and anhydrous ethanol (99%, SRL) were procured. Solutions were made with double-distilled water. Solution phosphate buffer (0.1 M PBS) was made of 0.1 M NaH_2PO_4 and 0.1 M Na_2HPO_4. The pH of 0.1 M PBS was adjusted using 1 M HCl or 1 M KOH. Electrochemical tests were carried out on the CHI-840b electrochemical workstation. Glassy carbon electrodes (GCEs) were polished with an alumina slurry of particle size 0.3 and 0.05 μm, and then ultrasonically washed in anhydrous ethanol and double-distilled water for 3 min each.

2.2 Separation of CTP

The HSP was determined by a dissolution test: 0.1 g of CTP was placed in a stoppered test tube, and after that 1 mL of different organic solvents were added to each stoppered test tube. Dissolution was observed, and the dissolved ones were recorded as "1" and the undissolved and partially dissolved ones were recorded as "0". The HSP of all solvents and CTP was distributed in a sphere. The center of the sphere was the optimal HSP of the organic solvents obtained from the simulation. Ethanol and toluene were selected as extractants. Coal pitch was extracted step-by-step to obtain CTPPI and CTPSI in turn. Based on the HSPIP, the solubility parameters of CTP have been published.[28]

2.3 Compound of CTPPI-PC material and CTPSI-PC modified GCE

Specific steps were used to make CTPSI-PC. Briefly, CTPSI, KOH, and silica were mixed and placed in containers to grind completely. After that, the CTPSI composite was carbonized in a N_2-atmosphere tube furnace at a heating rate of 5 °C min^{-1}. Then, the materials were annealed for 3 h at 800 °C in a N_2 environment. To maintain stability, the material was washed with a 1 M HCl solution and 1 M NaOH solution, which removed silica and stayed neutral. Finally, samples were dried at 90 °C for 10 h and labeled "CTPSI-PC". In addition, CTP-PC- and CTPPI-PC-modified electrodes were synthesized under identical conditions for comparison with the CTPSI-PC electrode (Fig. 1).

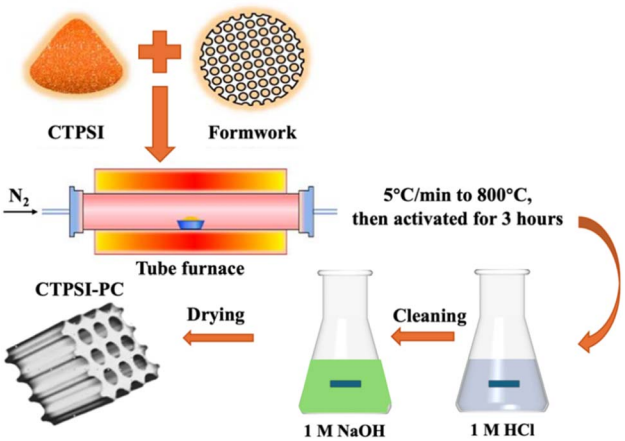

Fig. 1 Synthesis of CTPSI-PC.

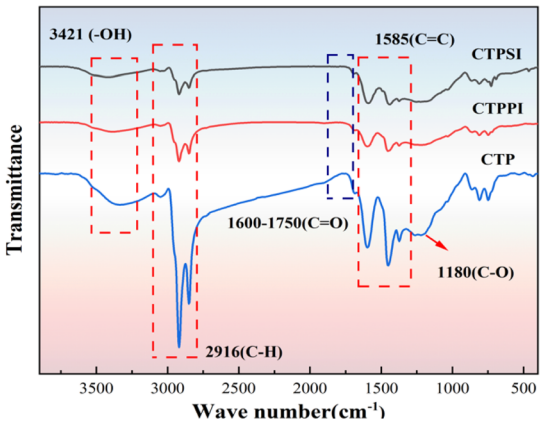

Fig. 2 FT-IR spectra of CTP, CTPPI and CTPSI.

3 Results and discussion

3.1. FT-IR spectroscopy

To evaluate the composition adjustment of CTP by different solvents, FT-IR spectroscopy was carried out on the three carbon sources of CTP, CTPPI, and CTPSI respectively. As shown in Fig. 2, the molecular structures of the three samples were quite different. An –OH stretching vibration absorption peak appeared at the wave number of 3421 cm^{-1}, and the strength of the –OH peak decreased with an increase in the extraction stage. This finding indicated that CTPSI contained fewer hydroxyl groups compared with the other two samples. At 2916 cm^{-1}, 1585 cm^{-1}, and 1434 cm^{-1}, fatty C–H stretching bending vibration absorption peaks and C=C skeleton stretching vibration absorption peaks appeared. With stepwise extraction, the strength of aromatic C–H (of 2916 cm^{-1}) weakened, indicating that the condensation degree of the aromatic ring gradually increased, and the hydrogen content gradually decreased. At wave numbers 1600 to 1750 cm^{-1}, as the extraction order increased, the spectral band gradually widened, representing the stretching vibration of C=O on ester or carboxyl groups, and the peak of wave number 1180 cm^{-1} was attributed to C–O in the ester. In the range of wave numbers 880–680 cm^{-1}, three types of C–H bending vibration characteristic peaks on the benzene ring (740 cm^{-1}, 798 cm^{-1}, and 871 cm^{-1}) were observed, which decreased with an increase in extraction order. In summary, the hydrogen and oxygen contents gradually decreased, the degree of aromatic ring condensation increased, and the molecular weight gradually increased, eliminating the lightweight components in CTP and making it a better carbon precursor.

3.2. Characterization of the ESI-PC composite

To characterize the morphology and structure of the synthesized CTPSI-PC material, SEM and TEM were done. Fig. 3a is the SEM image of CTP, which did not have a porous structure. Fig. 3b is the SEM image of the CTPSI-PC material, which had a dense porous structure on the surface and uneven distribution of pore sizes. To validate the SEM results further, TEM was used to analyze the material (Fig. 3c). Many pore structures were clearly distributed on the surface of the material, further supporting the results of SEM. In summary, CTPSI-PC material had a high specific surface area and was a typical porous carbon material.

Fig. 4a shows the N_2 adsorption–desorption isotherm curve of CTPSI-PC material. It can be observed that it had a typical type-IV adsorption–desorption contour line for temperature and related subjects. In the range 0.4–0.7, there was an H2-type hysteresis loop of typical columnar pores, indicating that it had a mesoporous pore structure. Fig. 4b shows the pore-size distribution of the sample. The pore size of the material was relatively uniform, with a concentrated average pore-size distribution and many mesoporous structures. The main pore-size distribution was around 2–20 nm. A mesoporous structure facilitates rapid electron transfer, improves the performance of carbon materials, and enables CTPSI-PC materials to have better electrochemical performance.

The degree of graphitization of CTPSI-PC material was studied using XRD and Raman spectroscopy. As shown in Fig. 5a, strong and sharp diffraction peaks could be observed near 30° and 60°. Near 43°, a weak and broad diffraction peak was observed, corresponding to the (002), (100), and (110) reflection surfaces, indicating that CTPSI-PC had a high degree of graphitization.[36] Fig. 5b shows the Raman spectrum of CTPSI-PC. The D and G peaks were located at 1332 cm^{-1} and 1587 cm^{-1}, respectively, and the 2D peak appeared around 2918 cm^{-1}. The presence of the D band indicated numerous defects in the CTPSI-PC material, and the G and 2D bands denoted a high degree of graphitization. The I_D/I_G ratio was calculated to be 1.04. If the ratio is >1, it denotes a good graphite

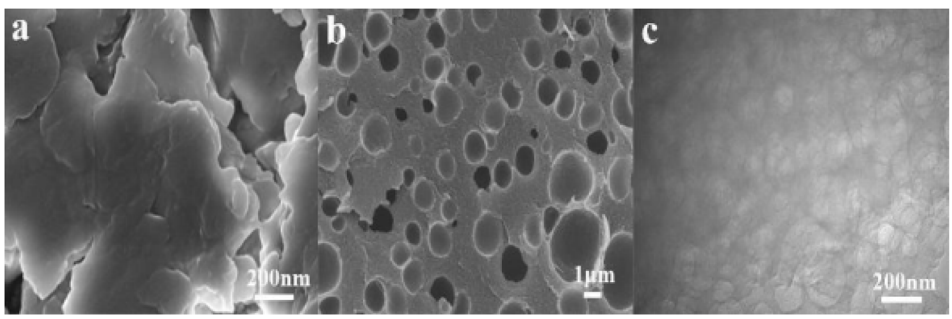

Fig. 3 (a) SEM of CTP. (b) SEM of CTPSI-PC. (c) TEM of CTPSI-PC.

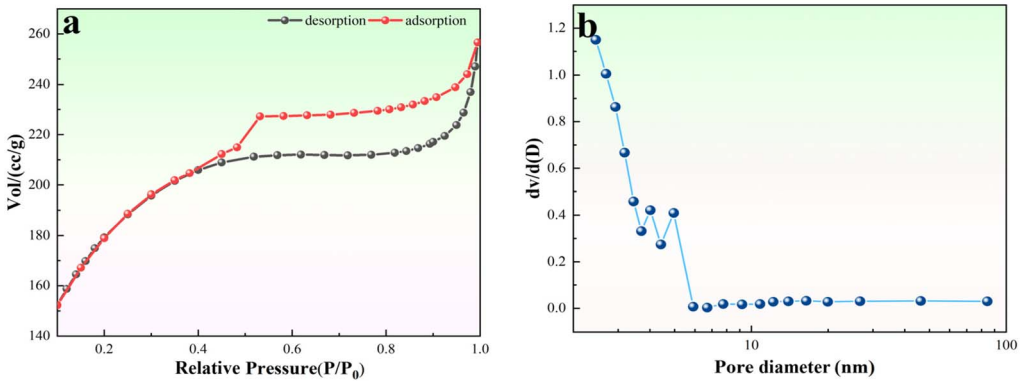

Fig. 4 (a) Adsorption and desorption isotherm curve of CTPSI-PC. (b) Pore-size distribution of the material.

structure. The characterizations stated above confirmed the graphene or graphene-like structure of the CTPSI-PC material.[37]

3.3 Electrochemical behavior of carmine at different electrodes

To compare the electrocatalytic performances of carmine at different electrodes, CV was carried on bare GCE, CTPPI-PC/GCE, CTP-PC/GCE and CTPSI-PC/GCE in 0.1 M PBS at a pH of 1.0. Fig. 6a shows that on bare GCE, no electric signal appeared from carmine (curve GCE). CM showed reversible redox behavior on CTP-PC/GCE, CTPPI-PC/GCE and CTPSI-PC/GCE. The CM redox peak current of the CTPSI-PC-modified electrode was far greater than that for the other GCE. These results showed that CTPSI-PC had an excellent electrocatalytic effect and CTPSI-PC/GCE had excellent sensitivity to CM. Hence, the proposed CTPSI-PC/GCE was chosen for additional studies of CM detection.

The electrochemical impedance spectroscopy (EIS) of various electrodes in 5 mmol L^{-1} $K_3[Fe(CN)_6]/K_4[Fe(CN)_6]$ solution containing 0.1 mol L^{-1} KCl solution was undertaken (Fig. 6b). The Nyquist plot of the electrochemical impedance spectrum contained a semicircular part at high frequency and a linear part at low frequency, which represents the electron transfer dynamics of the redox probe on the electrode surface. Bare GCE had a large semicircle and a straight line featuring the diffusion-limiting step of the $K_3[Fe(CN)_6]/K_4[Fe(CN)_6]$ processes. After the GCE was modified with CTP/PC, CTPPI-PC, or CTPSI-PC, the semicircle diameter decreased, meaning that these conductive materials facilitated electron transfer. The EIS curve for CTPSI-PC/GCE exhibited a straight line, which revealed that the electron-transfer kinetics of the redox probe were so fast that the semicircle disappeared. This finding indicated that the CTPSI-PC materials had high conductivities.

3.4 Effect of scan rate

Kinetic studies of the electrode reactions were investigated using CV of CTPSI-PC/GCE at different scan rates in 0.1 M PBS containing 100 μM CM at pH = 1.0. Fig. 7a reveals the CV curves of CM at a CTPSI-PC-modified GCE with scan rates ranging from 10 to 200 mV s^{-1}. The peak current of CM increased linearly with increasing electrode reaction scan rates, and plots of the relationship between peak current and scan rates were drawn. Moreover, the peak current of CM varied linearly with the scan rate, and the regression equations were $I_{pa} = -0.2407\nu - 2.6807$ (μA, mV s^{-1}, $R = 0.9932$) and $I_{pa} = 0.2446\nu + 2.1361$ (μA, mV s^{-1}, $R = 0.9971$). These data demonstrated that the redox reaction of CM on CTPSI-PC/GCE was an adsorption-controlled process.[38]

3.5 Effect of pH

The pH of the supporting electrolyte solution (PBS in our case) directly affects the form of the test substance and the

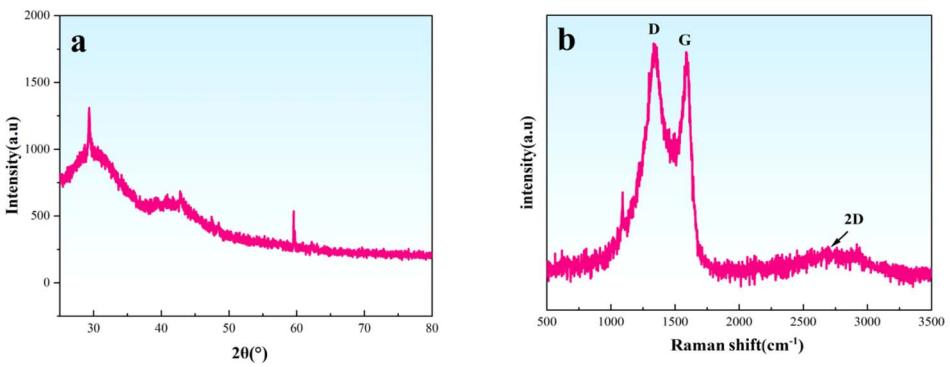

Fig. 5 (a) XRD spectrum of CTPSI-PC. (b) Raman spectrum of CTPSI-PC.

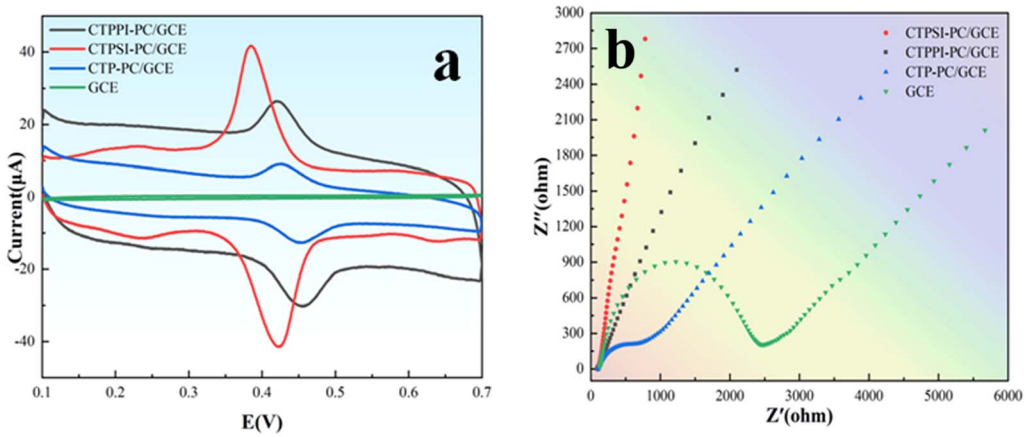

Fig. 6 (a) CV curves of CTP-PC/GCE, CTPPI-PC/GCE, CTPSI-PC/GCE and GCE in 0.1 M PBS containing 100 μM CM, scan rate = 100 mV s^{-1}. (b) EIS curves of different electrodes.

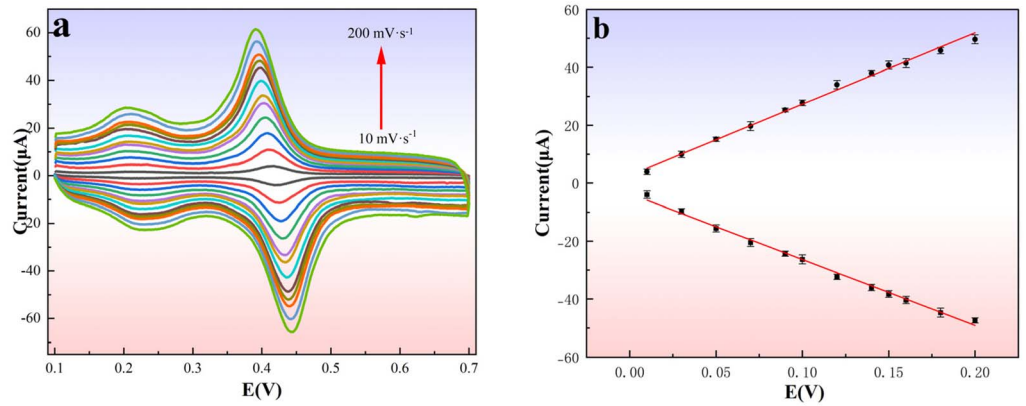

Fig. 7 (a) CV curves of CTPSI-PC/GCE with different ratios in 0.1 M PBS containing 100 μM CM, pH = 1.0. (b) Linear relationship between sweep speed and peak current.

conductivity of the electrochemical reaction system, thereby affecting the electrochemical signal. To improve the response sensitivity of CM, the pH of the solution was optimized. Fig. 8a shows the LSV curves of CM at different pH values (1.0, 2.0, 3.0, 4.0, 5.0) on CTPSI-PC/GCE. As shown in Fig. 8a, the peak current gradually decreased with an increase in pH. In Fig. 8b, the peak current was highest when pH = 1.0, which was attributed to the redox of CM on the modified electrode. Also, the azo group on the CM molecule was reduced to N–N– under strong acid conditions; the more H^+ content, the faster the reaction rate, and the stronger the current response. With an increase in pH, the lower the H^+ content, the weaker was the reaction. In addition, as shown in Fig. 8c, the peak potential shifted in the negative direction and there was a linear relationship between the peak potential and pH. In the linear regression equation E_{pa} (V) = −0.0529 pH + 0.5045 (R = 0.9925), the slope of the line in the equation was 52.9 mV pH^{-1}. This was close to −59 mV pH^{-1} in the Nernst equation at 25 °C, indicating that the same number of protons and electrons participated in the reversible electrochemical redox process of CM, and the proton concentration in strong acid solution was high. Hence, an electrode reaction could occur readily, so pH = 1.0 was selected as the best pH. The mechanism of the electrochemical reaction of IC at the surface of PSMCPE is shown in Fig. 9.

3.6. Analytical performance for of carmine determination

Compared with other methods of electrochemical detection, LSV technology has higher sensitivity, with a pH of 1.0 and a scanning speed of 100 mV s^{-1} denoting optimal test conditions for our study. Under a scan potential of 0.2–0.6 V, we used LSV to study CTPSI-PC/GCE for the detection of different concentrations of CM (10, 20, 30, 50, 70, 90, 110, 130, 150, and 200 μM), and determined the correlation linear relationship (Fig. 10a). The LSV curve showed that when the CM concentration increased from 10 μM to 200 μM, the peak current increased accordingly. According to Fig. 10b, there was a good linear relationship between the CM concentration in the range 10–200 μM. The linear equation was I_{pa} (μA) = −0.45159C (μM) − 4.0100 (R = 0.9942), sensitivity was 5.7324 A L cm^2 mol^{-1}, and the limit of detection (LOD) was 0.017 μM. These data indicated that CTPSI-PC/GCE had a high sensitivity to CM. According to Table 1, compared with other reported methods for detecting CM, the electrochemical sensor constructed using CTPSI-PC material had higher sensitivity and lower

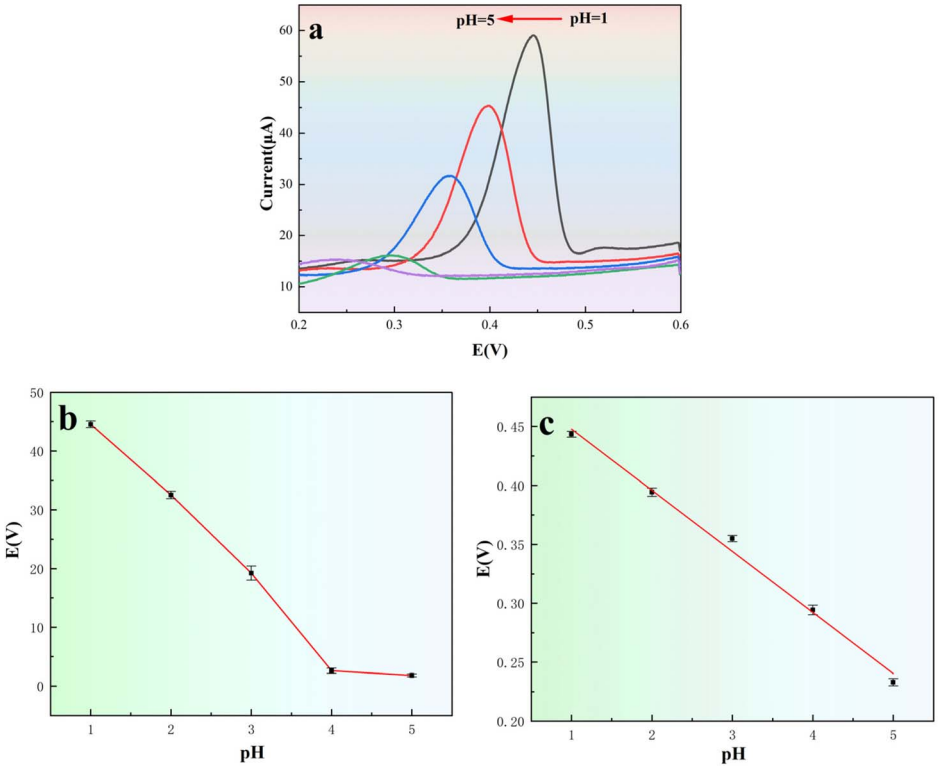

Fig. 8 (a) Effect of PBS with different pH values on the peak current and peak potential of CM. (b) Relationship between different pH values and peak current. (c) Linear relationship between different pH values and peak potential.

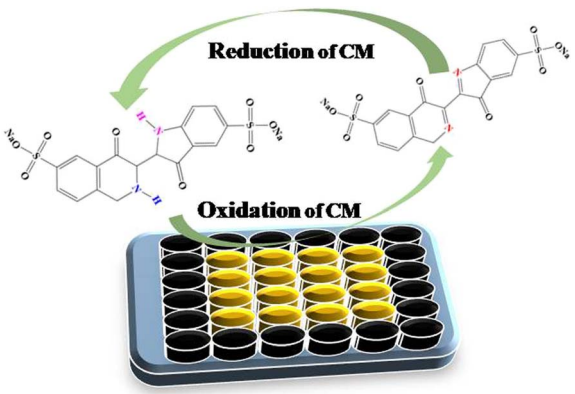

Fig. 9 Electrochemical reaction of CM on the modified electrode.

LOD and better application prospects. Besides, Table 1 lists the LOD for CM recorded at different electrodes reported by other researchers. In comparison with electrochemical approaches described previously, the constructed sensor had a wide linear range and lower LOD.

3.7. Repeatability, reproducibility, and stability of CTPSI-PC-modified GCE

LSVs verified the reproducibility of CTPSI-PC/GCE. Ten versions of CTPSI-PC/GCE were constructed for use in carmine analyses, and the relative standard deviations (RSD) was 0.90%, respectively. Furthermore, repeatability was investigated by measuring the same electrode five times, with the RSD of carmine being 2.73%. The electrochemical performances of CTPSI-PC/GCE was determined after 15 days of storage at room temperature. The oxidation peak current of carmine was 1.43% of the RSD, indicating that the constructed carmine sensor has good reproducibility, repeatability, and stability.

3.8. Interference studies

Some interfering chemicals were added to the test to confirm the anti-interference property of CTPSI-PC/GCE. A detection of 10 μM carmine in 0.1 M PBS (pH = 1.0) was explored. The data show that adding a tenfold excess of various interfering ions (blank, Ca^{2+}, K^{+}, Na^{+}, Mg^{2+}, NH^{4+}, Br^{-}, Sr^{2+}, Ba^{2+}, $CO_3{}^{2-}$, $HCO_3{}^{-}$, Cl^{-}, $SO_4{}^{2-}$, $NO_3{}^{-}$) has no significant effect on carmine detection. For the detection of carmine, the relative error caused by interfering compounds was ±5%. Fig. 11 shows that the competitors had no effect on the detection of carmine, indicating that the constructed sensor had a high selectivity for carmine.

3.9. Analyses of real samples

CTPSI-PC/GCE was used to assess the practical application performance of the developed sensor. We measured the CM concentration in an oilfield water sample using a standard addition procedure (*i.e.*, CM was detected in a real sample). Following the addition of a known quantity of carmine to the

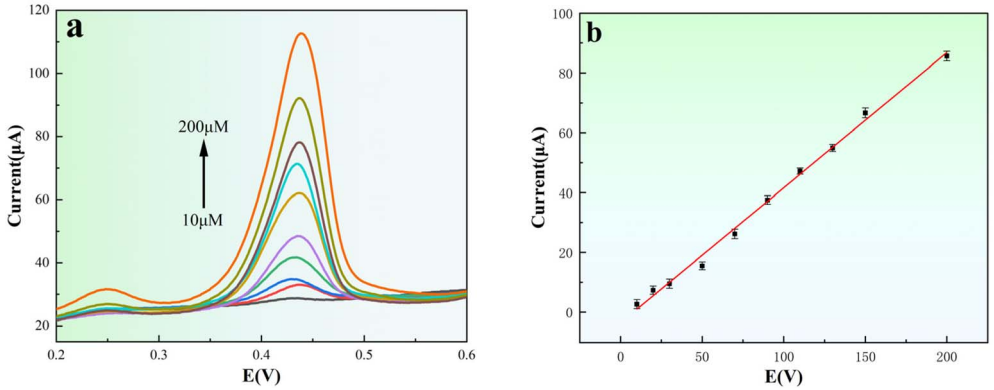

Fig. 10 (a) LSV curves of CM at CTPSI-PC/GCE (0.1 M PBS, pH = 1.0) for different CM concentrations (10, 20, 30, 50, 70, 90, 110, 130, 150 and 200 μM). (b) Linear relationship between CM concentration and peak current.

Table 1 Comparison of CM determinations between the present work and reported methods

Electrode	Method	Range (μM)	Detection limit	Report
ALMCPE[a]	CV	20–500 μM	0.78 μM	39
Y_2O_3@GPE[b]	DPV	5–300 μM	0.17 μM	40
P(GA)LMWCNTPE[c]	DPV	5–50 μM	0.36 μM	41
PSMCPE[d]	DPV	0.3–3.5 μM	0.13 μM	42
CTPSI-PC/GCE	LSV	10–200 μM	0.017 μM	This work

[a] Alanine-modified carbon paste electrode. [b] Yttrium oxide (Y_2O_3) nanoparticles to modify a graphite paste electrode. [c] Poly(glutamic acid)-layered multiwalled carbon nanotube paste electrode. [d] Poly(serine)-modified carbon paste electrode.

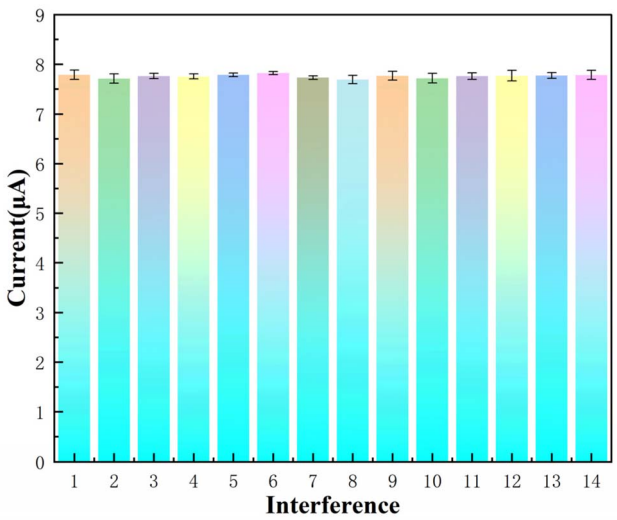

Fig. 11 LSV response of CM in 0.1 M PBS solution at pH = 5.0 at CTPSI-PC/GCE for different interfering compounds.

test system (Table 2), the recovery was 99.4% and 103.2%. These findings showed that the constructed sensor could detect CM quickly in oilfield water circumstances. To verify the accuracy of the constructed electrochemical sensor, high-performance liquid chromatography (HPLC) was used to test the known

Table 2 Detection of CM in oilfield water samples

Sample	Added (μM)	Found (μM)	Recovery (%)
1	10	10.13	101.3
2	20	20.63	103.2
3	40	40.60	101.5
4	60	60.57	100.9
5	100	99.53	99.4

CM content in a real sample. With a CM concentration of 20 mg L^{-1}, the LOD of HPLC detection was 19.998 mg L^{-1}, and recovery rate was 99.99%. The relative error between the HPLC result and the constructed electrochemical sensor at the same concentration was 3.2%, indicating that the electrochemical sensor had high accuracy. This sensor has good application prospects for the detection and analyses of CM content in actual samples.

4. Conclusions

A GCE-modified with porous carbon derived from CTPSI-PC was fabricated and electrochemical performances evaluated. The electrochemical behavior of CM on CTPSI-PC/GCE was characterized using CV and LSV, revealing rapid electron transfer kinetics and outstanding electrocatalytic activity towards CM. Under optimal conditions, the CTPSI-PC-modified sensor exhibited excellent analytical performance, including high sensitivity, a broad linear detection range (10–200 μM), a low LOD of 0.01 μM (S/N = 3), as well as exceptional repeatability and reproducibility. The sensor also demonstrated superior selectivity in the presence of common interfering species, making it well-suited for the reliable detection of CM in complex matrices. The functionality of the sensor was verified by quantifying CM in authentic oilfield water samples under controlled analytical conditions, achieving consistent recovery rates and high precision. These findings confirm the potential of the sensor as candidate technology for practical

implementation, pending validation in operational field environments and system-integration studies.

Data availability

The data supporting the findings of this study are available from the corresponding author upon reasonable request.

Conflicts of interest

The authors have no conflict of interest to declare.

Acknowledgements

Funding for this work was supported by National Natural Science Foundation of China (22168038).

References

1 S. Maiti, N. K. Choudhary, K. R. Gore and S. D. Kulkarni, *J. Pet. Explor. Prod. Technol.*, 2025, **15**(2), 30.
2 A. Kumar and C. Sharma, *J. Sep. Sci.*, 2022, **45**, 78–93.
3 Q. Liu, S. Diao and T. Li, *Complex Hydrocarbon Reservoirs*, 2016, vol. 9, pp. 65–68.
4 P. A. Pushpanjali, J. G. Manjunatha and N. Hareesha, *J. Electrochem. Sci. Eng.*, 2021, **11**, 161–177.
5 T. Ban, C. L. Li and Q. Wang, *J. Mol. Liq.*, 2018, **271**, 265–273.
6 Y. J. Cao, C. Y. Lu, Z. W. Zhang, Z. Wang, Y. H. Kang, T. T. Yang, G. H. Liu, X. Y. Wei and H. C. Bai, *ACS Omega*, 2022, **7**(27), 23342–23342.
7 J. H. Huang, L. Shao, Y. Q. Zhang, Y. J. Zhang, K. Wang, J. Ma, E. Drioli and X. Q. Cheng, *Chem. Eng. Sci.*, 2022, **263**, 118071.
8 N. Wang, B. M. Xu, X. H. Wang, J. Y. Lang and H. Zhang, *J. Mol. Liq.*, 2022, **366**, 120294.
9 M. Mihalovits, *J. Mol. Liq.*, 2022, **364**, 119911.
10 X. X. Yang, S. Zhao, Z. Z. Zhang, Y. Chi, C. M. Yang, C. T. Wang, Y. Z. Zhen, D. J. Wang, F. Fu and R. A. Chi, *J. Colloid Interface Sci.*, 2022, **614**, 298–309.
11 D. Yu, L. H. Zhou, J. Hu, C. J. Peng and H. L. Liu, *J. Solid State Electrochem.*, 2019, **23**, 2455–2464.
12 C. Czosnek, W. Ratuszek, J. F. Janik and Z. Olejniczak, *Fuel Process. Technol.*, 2002, **79**, 199–206.
13 F. Dong, C. Liu, M. J. Wu, J. N. Guo, K. X. Lo and J. L. Qiao, *ACS Sustainable Chem. Eng.*, 2019, **7**, 8587–8596.
14 N. Ali, H. Zaman, W. Zaman and M. Bilal, *Mater. Chem. Phys.*, 2020, **242**, 122564.
15 B. Qin, Q. Wang, X. H. Zhang, X. L. Xie, L. E. Jin and Q. Cao, *Electrochim. Acta*, 2018, **283**, 655–663.
16 S. Venkatram, C. Kim, A. Chandrasekaran and R. Ramprasad, *J. Chem. Inf. Model.*, 2019, **59**, 4188–4194.
17 C. R. Li, H. R. Wang, W. Huang, T. Wen, J. K. Xu, J. B. Ouyang and C. T. Zhang, *J. Mol. Liq.*, 2021, **339**, 116733.
18 S. Yu, Y. Cheng, W. C. Feng, W. G. Xing, H. C. Li and F. M. Xue, *J. Mol. Liq.*, 2021, **339**, 116750.
19 W. F. Zhang, Z. H. Huang, G. P. Cao, F. Y. Kang and Y. S. Yang, *J. Phys. Chem. Solids*, 2012, **73**, 1428–1431.
20 G. L. Zhang, T. T. Guan, J. L. Qiao, J. L. Wang and K. X. Li, *Energy Storage Mater.*, 2020, **26**, 119–128.
21 W. Zhi, *Adv. Mater. Res.*, 2013, **631–632**, 486–489.
22 Y. Yang, Z. P. He, Y. Liu, S. L. Wang, H. G. Wang and G. S. Zhu, *Appl. Surf. Sci.*, 2021, **565**, 150579.
23 Y. D. Li, X. Q. Chen, Z. H. Zeng, Y. Dong, S. H. Yuan, W. Q. Zhao, F. Jiang, Y. Yang, W. Sun and P. Ge, *ACS Appl. Energy Mater.*, 2022, **5**, 7874–7888.
24 P. R. Romel-Antonio, E. L. Carlos, P. R. Karem-Tatiana and G. B. Mauricio, *CT&F, Cienc., Tecnol. Futuro*, 2020, **10**, 27–38.
25 A. Chieli, J. Sanyova, B. Doherty, B. G. Brunetti and C. Miliani, *Spectrochim. Acta, Part A*, 2016, **162**, 86–92.
26 E. Svensson Grape, T. Willhammar and A. K. Inge, *Cryst. Growth Des.*, 2025, **25**, 4100–4105.
27 F. J. Jia, H. T. Li, Z. M. Liu, Y. Li, X. Ma, G. Q. Zhang and Q. H. Zhang, *J. Environ. Chem. Eng.*, 2024, **12**, 113560.
28 N. Yalikun, H. Z. Gong, C. F. Liu and Y. S. Zhang, *Microchem. J.*, 2024, **207**, 111769.
29 J. Baranwal, B. Barse, G. Gatto, G. Broncova and A. Kumar, *Chemosensors*, 2022, **10**(9), 363.
30 X. Y. Zhao, J. H. Ding, W. L. Bai, Y. F. Wang, Y. J. Yan, Y. Cheng and J. K. Zhang, *J. Electroanal. Chem.*, 2018, **824**, 14–21.
31 G. Tigari, J. G. Manjunatha, E. S. D'Souza and N. Sreeharsha, *ChemistrySelect*, 2021, **6**, 2700–2708.
32 P. A. Pushpanjali and J. G. Manjunatha, *Electroanalysis*, 2020, **32**, 2474–2480.
33 A. B. Monnappa, J. G. Manjunatha and A. S. Bhatt, *ACS Omega*, 2020, **5**, 23481–23490.
34 P. A. Pushpanjali, J. G. Manjunatha and M. T. Srinivas, *FlatChem*, 2020, **24**, 100207.
35 J. G. Manjunatha, *Anal. Bioanal. Electrochem.*, 2020, **12**, 893–903.
36 Y. Ma, Structure Regulation and Electrochemical Performance of Asphalt-based Porous Carbon, M.Eng thesis, Tiangong University, 2016, in Chinese.
37 J. Li, Controllable Preparation of Carbon-based Electrode Materials and Their Application in Electrochemical Energy Storage, Ph.D thesis, University of Science and Technology of China, 2022, in Chinese.
38 Y. Xie, W. Zhou, J.-W. Yin, Y. Li, C.-Y. Lai, J.-H. Lai, Z.-J. Zhu, X.-G. Yi, L.-M. Liu and K. Salminen, *Diamond Relat. Mater.*, 2025, **155**, 112366.
39 S. Saipriya, J. G. Manjunatha, K. Bhimaraya, N. Ataollahi, S. A. Aldossari and E. S. D'Souza, *Monatsh. Chem.*, 2025, **156**, 407–418.
40 S. Dasgupta, A. H. M. T. Ahmed, I. Bhattacharjee, S. Firdoushi, D. Biswas, S. Mukherjee, B. Mondal, R. Bandyopadhyay and B. Tudu, *J. Food Compos. Anal.*, 2024, **135**, 106626.
41 M. Díaz-González, C. Fernández-Sánchez and A. Costa-García, *Electroanal*, 2002, **14**, 665–670.
42 N. Hareesha, J. G. Manjunatha, B. M. Amrutha, P. A. Pushpanjali, M. M. Charithra and N. P. Subbaiah, *J. Electron. Mater.*, 2021, **50**, 1230–1238.